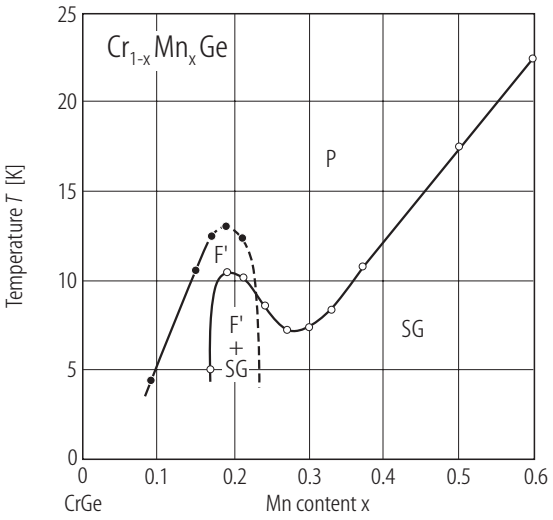

Fig. 20. $Cr_{1-x}Mn_xGe$. Magnetic phase diagram in temperature vs. composition plane proposed on the basis of detailed magnetic measurements [88S1]. P: paramagnetic state; SG: spin glass state; F': ferromagnetic or helical magnetic (for x = 0.19) state [94S1].

1.5.4.4 Mn alloys and compounds

Compounds of Mn with Si, Ge or Sn exhibit a variety of types of magnetic ordering. In particular, Mn_3Sn, a triangular antiferromagnet with uncompensated remanent magnetic moment, has got much attention since [82T1, 82T2]. The sample dependence of the magnetic properties of this compound suggests a delicate energy balance. It should be mentioned also that the magnetism of the most Si-rich compound $MnSi_{1.75-x}$ seems to be left unclarified as a consequence of the sensitivity of the crystal structure to the preparation conditions. Note also that the composition $Mn_{11}Si_{19}$ belongs to this group. According to [86Y3] it has a "chimney-ladder" structure, in which the Mn atoms form a tetragonal arrangement (chimney) with lattice parameters a = 5.52 Å and c_{Mn} = 4.37 Å while the Si atoms occupy interstices of the Mn sublattice, forming a coupled helical arrangement (ladder) with a period c_{Si} around 4 c_{Mn} [86Y3]. The change of the ratio c_{Si}/c_{Mn} with x and temperature leads to a variety of long-period or rather incommensurate structures, which makes it difficult to understand the physical properties of this and also of the related ternary compounds.

Survey

Composition x	Properties	Figure	Table
$Mn_{0.912}Si_{0.088}$	$H_{hyp}(T)$	21	
Mn_3Si	$\omega(q)$	22	
$Mn_{2.8}Fe_{0.2}Si$	$\omega(q)$	23	
Mn_5Si_3	magnetic structure	24	4
	$\sigma(H;T)$	25	
MnSi	$T_1^{-1}(T)$ for muon, ^{55}Mn	26	
	$\rho(T;p)$	27	
	neutron paramagnetic scattering $(\hbar\omega,Q;T)$	28	

	Composition x	Properties	Figure	Table
$MnSi_{1.75}$		$\sigma(H)$	29	
Mn_3SnC		$\sigma(T)$, $\chi_m^{-1}(T)$, $a(T)$	30	4
		$\Delta T_C(p)$	31	
		magnetic structure	32	
Mn_3Ni_2Si		$\chi_g(T)$, $I_{ND}(T)$	33	4
		magnetic structure	34	
$Mn_6Ni_{16}Si_7$		$\chi_g(T)$, $\chi_g^{-1}(T)$	35	4
		magnetic structure	36	
$Mn_3Cr_3Ni_{16}Si_7$		$\chi_g(T)$, $\chi_g^{-1}(T)$	35	4
εMn_3Ge	23.5, 23.0 at% Ge	$\sigma(T;H)$, $\sigma(H)$, $\sigma(T)$	37, 38	
$\varepsilon_1 Mn_3Ge$	23.5 at% Ge	$\sigma(H;T)$, $\sigma(T)$	39	
$\zeta_1 Mn_{2.6}Ge$	27.8 at% Ge	$\sigma(T;H)$	40	
ζ	28 at% Ge	thermal expansion $\Delta l/l(T)$	41	
		$K_1(T)$	42	
ζ_1	$Mn_{5.11}Ge_2$	crystal structure	43	5
ζ_2	Mn_5Ge_2	crystal structure	44	5
κMn_5Ge_2		$\sigma(T)$	45	5
		crystal structure, magnetic structure	46	
ηMn_5Ge_3		$\sigma(T)$	47	5
		$\lambda_{001}(T)$, $\lambda_{100}(T)$	48	
$\theta Mn_{11}Ge_8$		$\sigma(T;H)$, $\sigma(H)$, $H_{th}(T)$ [1])	49, 50	5
		$\sigma(H;T)$, $H_{cr}(T)$, $\Delta\sigma(T)$	51	
		crystal structure	52	
$Mn_{1-x}Fe_xGe_4$ [2])	0	$\rho(T)$	53	6
	0...0.4	$\sigma(T;x)$, $\chi_g^{-1}(T;x)$	53	
$Mn_{1-x}Co_xGe_4$ [2])	0...0.3	$\sigma(T;x)$, $\chi_g^{-1}(T;x)$	54	
Mn_3Sn	$Mn_{3.6}Sn$	$\sigma(T)$, $\chi_g(T)$	55	7
	$Mn_{3.2}Sn$	magnetic structure	56	
		magnetic excitation spectra	57	
	$Mn_{3.2}Sn$	dispersion relations	58	
		$I_{ND}(T)$	59	
		ND satellite peak positions (T)	60	

	Composition x	Properties	Figure	Table
$(Mn_{1-x}Fe_x)_{3.25}Ge$	0.18, 0.22, 0.30	$\sigma_s(T)$	61	
	0...1	x-T magnetic phase diagram	62	
$(Mn_{1-x}Fe_x)_3Sn_{1-\delta}$		x-T magnetic phase diagram	63	
$Mn_7(Sn_{1-x}Ge_x)_4$	0, 0.5	$\sigma(T;H)$	64	
	0...0.5	$\sigma(T;x)$	65	
	0...0.5	$T_C(p;x)$	66	
	0, 0.1	$T_{tr}(p;x)$	66	
$Mn_{1-x}Fe_xSn_2$		x-T magnetic phase diagram	67	
		$H_{hyp}(x;T)$	68	
$Mn_{1-x}Co_xSn_2$		x-T magnetic phase diagram	69	

[1]) Threshold magnetic field for spin flop.
[2]) High-pressure synthesized compounds.

For Tables 4 and 5 see p. 16 and 17

Table 6. Magnetic and related properties of high-pressure synthesized compounds $MnGe_4$ and $CoGe_4$ [90T1].

	$MnGe_4$	$CoGe_4$
Crystal structure	tetragonal	cubic
a [Å]	11.03	10.99
c [Å]	5.598	
Magnetism	ferro	Pauli para $\chi_g = 5 \cdot 10^{-7} cm^3 g^{-1}$
T_C [K]	340	
Θ [K]	349	
p_{Mn} [μ_B/Mn]	1.2	
p_{eff} [μ_B/Mn]	2.83	
Synthesizing conditions		
p [kbar]	55	60
T [°C]	600…700	600…700
t [h]	2	2
Decomposition temperature at ambient pressure [°C]	270	380

Table 4. Supplement to Table 5 in LB III/19C, subsect. 1.5.4.4. Magnetic and related properties of Mn_5Si_3 [92B2], Mn_3SnC [78F2], Mn_3Ni_2Si [90K2], $Mn_6Ni_{16}Si_7$ and $Mn_3Cr_3Ni_{16}Si_7$ [91K1].

	Mn_5Si_3		Mn_3SnC	Mn_3Ni_2Si	$Mn_6Ni_{16}Si_7$	$Mn_3Cr_3Ni_{16}Si_7$
Crystal structure	hexagonal D8$_8$ orthorhombic at low	temperature	cubic E2$_1$($CaTiO_3$ perovskite)	cubic $Fd\bar{3}m$	cubic($Mn_6Cu_{16}Si_7$) $Fm\bar{3}m$	cubic($Mn_6Cu_{16}Si_7$) $Fm\bar{3}m$
a [Å]	6.910	6.889	3.986 at 4.2 K [72F1]	10.756	11.009	11.010
b [Å]		11.901($\approx a\sqrt{3}$)				
c [Å]	4.814 at 300 K (hex)	4.805 at 4.2 K (ortho)				
Magnetism	antiferro		noncollinear ferro	antiferro	antiferro	antiferro
T_N [K]	99 [90M1]			215	205	165
T_C [K]			294 (first order)			
Θ [K]			– 1023 [72F1]		– 145	100
p_{Mn} [μ_B/Mn]	1.6(4d) 0.8(6g) at 67 K [90M1] 1.2(4d) 2.30,1.85, 0(6g) at 4.2 K		2.4 (Mn1, Mn2) 0.65 (Mn3)	0.57	2.7	1.8
p_{eff} [μ_B/Mn]					5.22	4.23
structure	canting angles [1]) at 4.2 K		Mn1 and Mn2 forms a square	Fig. 34	Fig. 36	Fig. 36
	θ	ϕ	configuration with 0.2 μ_B per	$p_{Ni} = 0$		$p_{Cr} = 0$
	116°	105° (4d)	Mn along [001].			
	70°	93° (6g)	Here Mn1, 2 and 3 are Mn on *a,*			
	21°	11°	*b* and *c* plane of perovskite unit			
	See Fig. 24.		cell.			
			See Fig. 32.			

[1]) θ: from *c* axis; ϕ: from *ac* plane. Moments are either parallel or antiparallel to the directions shown.

Table 5. Supplement to Table 6 in LB III/19C, 1.5.4.4. Magnetic and related properties of Mn_3Ge [88Y2], Mn_5Ge_2 [88Y1, 85Y1], Mn_5Ge_3 [90Y1], $Mn_{11}Ge_8$ [86Y1].

	Mn_3Ge		Mn_5Ge_2			Mn_5Ge_3	$Mn_{11}Ge_8$
Concentration range [at%Ge(x in Mn_xGe)]	22.7-24.0 (3.41-3.17) at 800°C		27.6-28.2 (2.62-2.55) at 800°C		28.6 (2.5)	37.2-37.7 [90m] (1.69-1.65)	42.1 (1.375)
Crystal structure {Phase}	T>515°C {ε} hexagonal $D0_{19}$ (Ni_3Sn)	T<515°C {ε_1} tetragonal $D0_{22}$ (Al_3Ti)	metastable at T<620°C {ζ} [90m] trigonal P3c1 Fig. 43{ζ_1}	P3c1 Fig. 44{ζ_2} [3])	T<690°C {κ} [90m] orthorhombic Ibam Fig. 46	{η} hexagonal $D8_8(Mn_5Si_3)$	T<796°C [90m] {θ} orthorhombic Pnam Fig. 52
a [Å]	5.343	no new data [2])	7.198	7.198	11.781	7.184	13.214
b [Å]					6.136		15.880
c [Å]	4.314 for 23.5at%Ge (x=3.26)		39.227 [87K1]	13.076 [87O1]	5.368 [84O2]	5.053 [90F1]	5.0905 at 295K [84O1]
Magnetism	antiferro with parasitic ferro		antiferro with parasitic ferro at 125K<T<T_C	315K<T<T_N	ferri	ferro	antiferro with parasitic ferro at 150K<T<T_N
T_N [K]	395 [71K1]		480	480			274
T_C [K]	365		225	480 [86Y2]	710	296	274
Θ [K]	–853						329
p_{Mn} [μ_B/Mn]		–4.7(2a) [1]) –3.0(2b) +1.9(4d) at 30 K [90Y1]			2.54(4b) 2.26(8f) –3.11(8j) at 13K [87Y1]	1.96(4d) 3.23(6g) [90F1]	
σ [Gcm^3g^{-1}]		12.6 at 4.2 K for 23.5 at%Ge [90Y1]					
p_s [μ_B/Mn]	0.007 at RT					2.60	0.05
σ_s [Gcm^3g^{-1}]					11.0 at 4.2 K	147.5 at 4.2 K	
p_{eff} [μ_B/Mn]	3.89						3.26
structure	triangular [83T1] $\sigma_s \perp c$	P-type ferri $p_{Mn} \parallel c$ [90Y1]	undetermined $\sigma_s \perp c$	$\sigma_s \parallel c$ in parasitic ferro regions [4])	N-type ferri; compensation at 395K $p_{Mn} \parallel b$ [87Y1]	$p_{Mn} \parallel c$	non-collinear antiferro $\sigma_s \parallel b$ at T>150K [4])

[1]) 0.06Mn+0.94Ge on 2a for 23.5 at%Ge.

[2]) Note that fct is equivalent to bct, but $a_{fct}=\sqrt{2}\,a_{bct}$.

[3]) Quenched specimen consists of domains of two subphases ζ_1 and ζ_2 making parallel intergrowth with common crystallographic axes.

[4]) Both transitions at 125 K for ζ_1 and 315 K for ζ_2 subphases are of the first order, as well as the one at 150 K for θ phase.

Table 7. Supplement to Table 7 in LB III/19C, subsect. 1.5.4.4. Magnetic and related properties of Mn_3Sn [86T1, 90B2]. Concentration range x in Mn_xSn: 3.2…3.7.

	Mn_3Sn
Crystal structure	hexagonal, $D0_{19}$ (Ni_3Sn)
a [Å]	5.665
c [Å]	4.531 for x = 3.34 [82T1]
Magnetism	antiferro with parasitic ferro
T_N [K]	420
p_{Mn} [μ_B/Mn]	2.75 at 7 K for x = 3.6 [87O2] 3.00 at 200 K for x = 3.2
p_s [μ_B/Mn]	0.1 at 4.2 K
structure	triangular first-order transition [87O2] at T_{t1} and another transition at T_{t2} T_{t1} = 150…270 K T_{t2} = 50…100 K $T_{t1} < T < T_N$: $p_{Mn} \perp c$, uncompensated WF $\sigma_s \perp c$ [1]) $T_{t2} < T < T_{t1}$: modulation along c with period of $12c$…$14c$, $\sigma_s \approx 0$ $T < T_{t2}$: large σ (5.3 G cm^3g^{-1}) $\parallel c$

[1]) 0.1…0.2 G cm^3g^{-1} dependent on x, thermal treatment [87O2, 87T2], and field cooling condition [86T1].

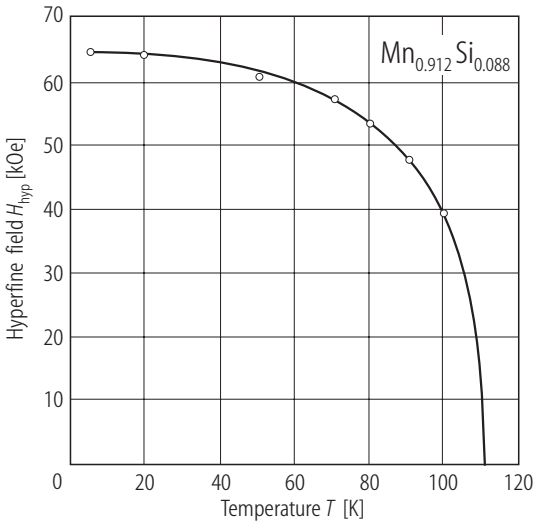

Fig. 21. $Mn_{0.912}Si_{0.088}$. Temperature dependence of hyperfine field H_{hyp} probed by ^{111}Cd in perturbed-angular-correlation experiments. Cd atoms are considered to occupy only 2a (Mn1) sites of A12 (αMn) structure [90D1].

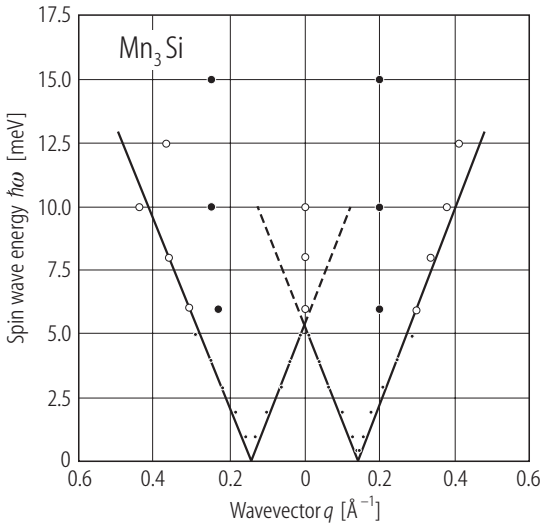

Fig. 22. Mn_3Si. Dispersion relation of the spin waves as studied through neutron inelastic scattering at 5.5 K. Peak positions in constant-E scan experiments are plotted in an energy transfer $\hbar\omega$ vs. q plane, q being the magnitude of the wave vector relative to commensurate point in reciprocal space. Open circles: longitudinal scan; solid circles: transverse scan. The slope of the straight lines is 37 meVÅ [87T3, 87T4].

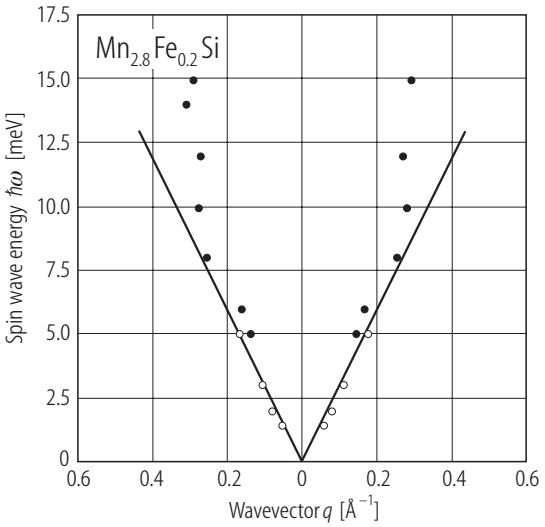

Fig. 23. $Mn_{2.8}Fe_{0.2}Si$. Dispersion relation of the spin waves as studied through neutron inelastic scattering at 7 K. Peak positions in constant-E scan experiment are plotted in an energy transfer $\hbar\omega$ vs. q plane, q being the magnitude of wave vector relative to the commensurate point in reciprocal space. Open circles: longitudinal scan; solid circles: transverse scan. The slope of the straight lines is 30 meVÅ [87T4].

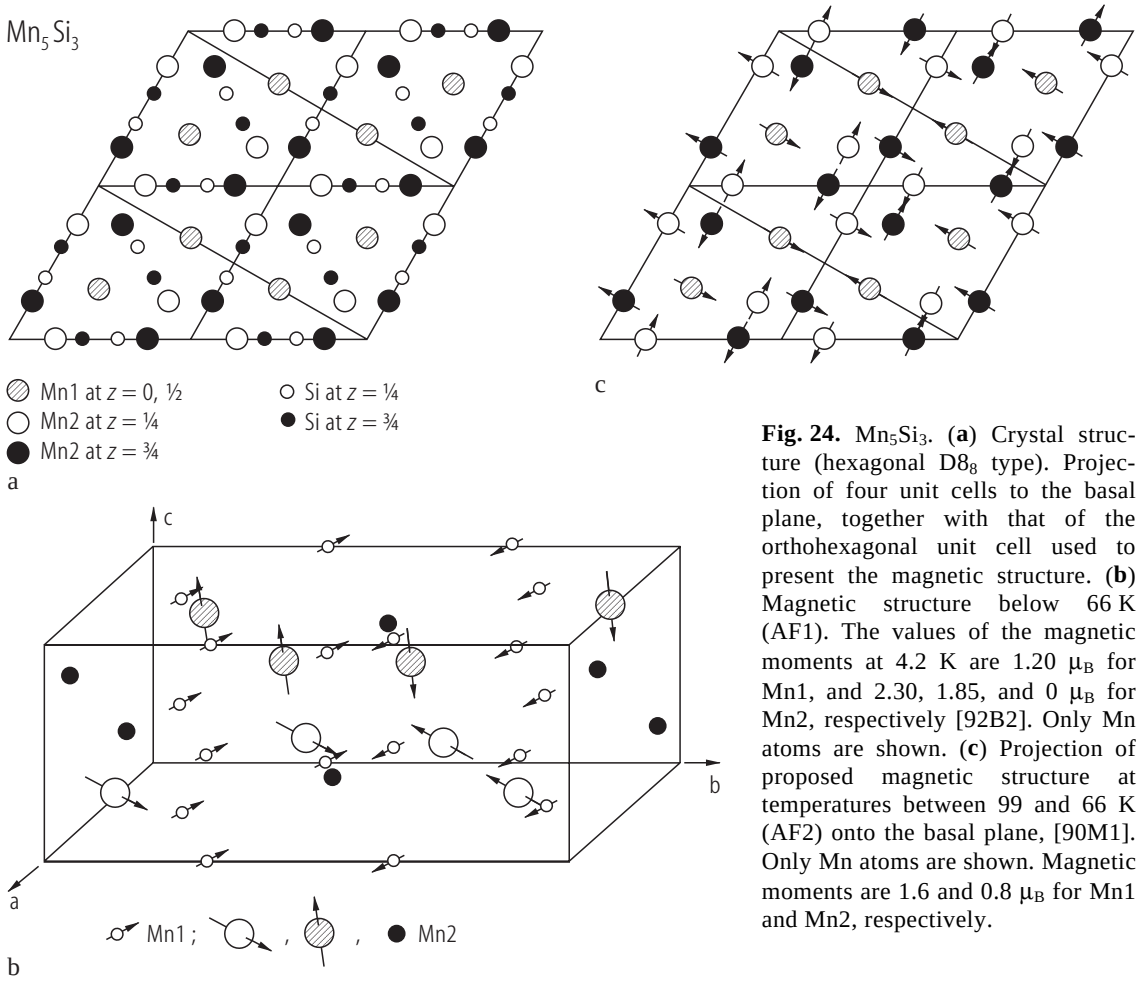

Fig. 24. Mn_5Si_3. (**a**) Crystal structure (hexagonal $D8_8$ type). Projection of four unit cells to the basal plane, together with that of the orthohexagonal unit cell used to present the magnetic structure. (**b**) Magnetic structure below 66 K (AF1). The values of the magnetic moments at 4.2 K are 1.20 μ_B for Mn1, and 2.30, 1.85, and 0 μ_B for Mn2, respectively [92B2]. Only Mn atoms are shown. (**c**) Projection of proposed magnetic structure at temperatures between 99 and 66 K (AF2) onto the basal plane, [90M1]. Only Mn atoms are shown. Magnetic moments are 1.6 and 0.8 μ_B for Mn1 and Mn2, respectively.

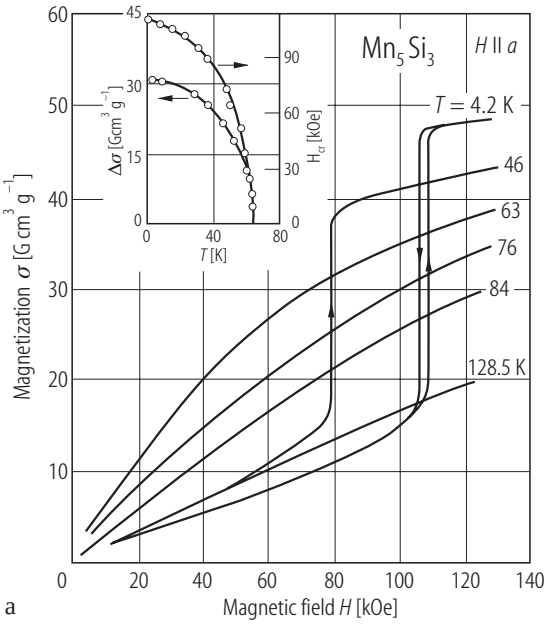

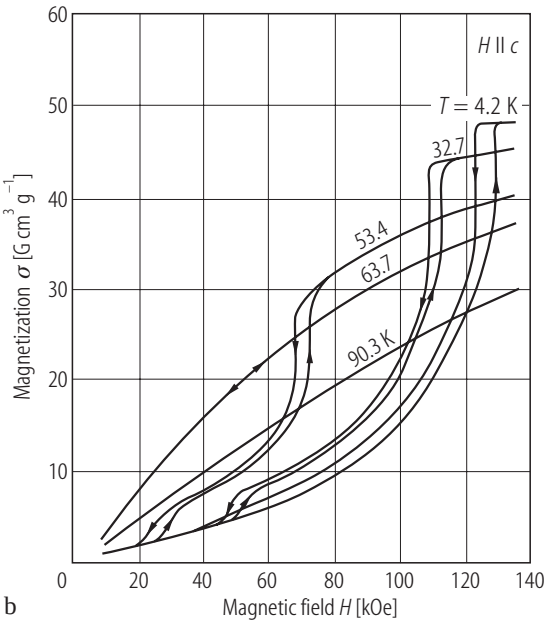

Fig. 25. Mn_5Si_3. Dependence of the mass magnetization σ on magnetic field H at various temperatures. The magnetic field is (**a**) along the a axis, and (**b**) along the c axis. Inset in (**a**) shows the temperature dependences of the critical field H_{cr} and of the jump in the magnetization $\Delta\sigma$ at H_{cr} [90V1].

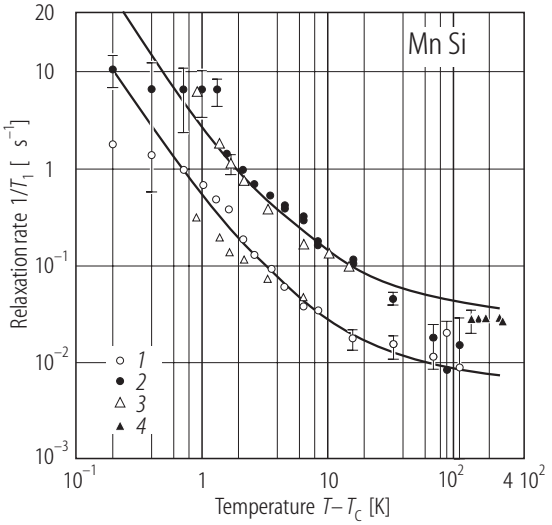

Fig. 26. MnSi. Temperature dependence of the spin-lattice relaxation rates for (*1*) muon ($1/T_1^{\mu}$) and (*2*) ^{55}Mn ($1/T_1^{Mn}$) [93K1, 90K1]. Earlier data (*3*) [87M1] and (*4*) [78Y1] have also been plotted.

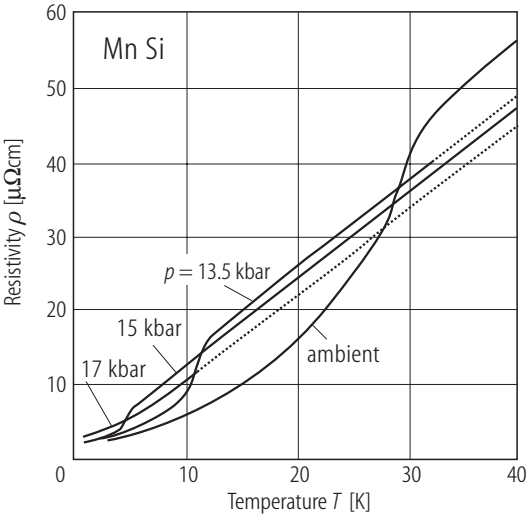

Fig. 27. MnSi. Temperature dependence of the electrical resistivity ρ under pressure. The shoulder in a curve corresponds to the Curie temperature for the helical itinerant ferromagnetism at the various pressures [93P1].

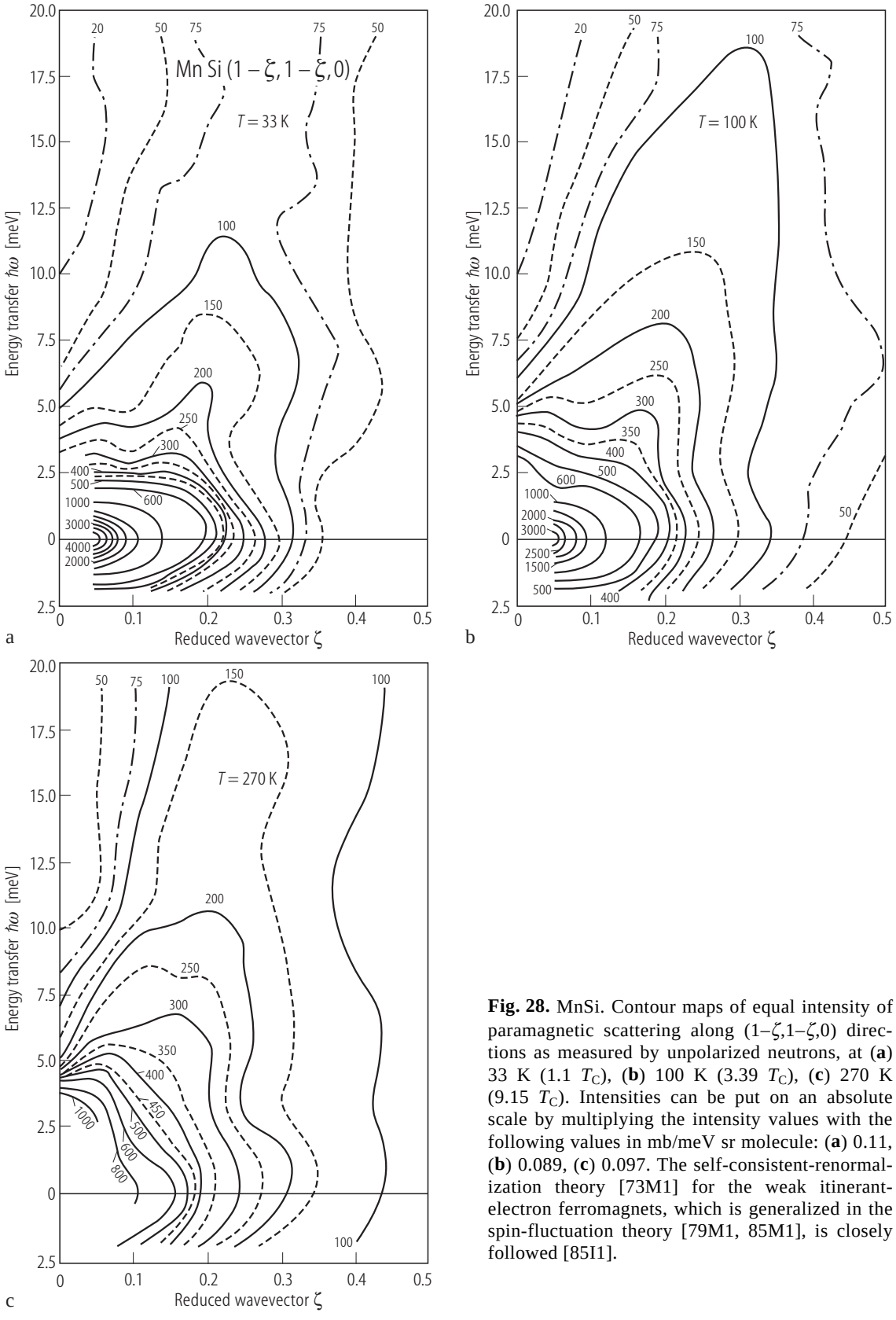

Fig. 28. MnSi. Contour maps of equal intensity of paramagnetic scattering along (1–ζ,1–ζ,0) directions as measured by unpolarized neutrons, at (**a**) 33 K (1.1 T_C), (**b**) 100 K (3.39 T_C), (**c**) 270 K (9.15 T_C). Intensities can be put on an absolute scale by multiplying the intensity values with the following values in mb/meV sr molecule: (**a**) 0.11, (**b**) 0.089, (**c**) 0.097. The self-consistent-renormalization theory [73M1] for the weak itinerant-electron ferromagnets, which is generalized in the spin-fluctuation theory [79M1, 85M1], is closely followed [85I1].

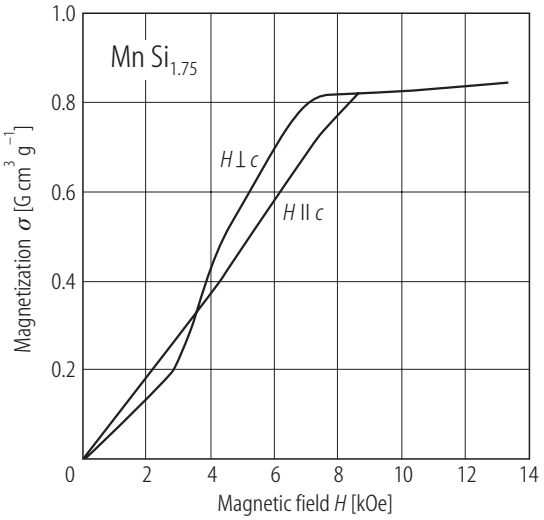

Fig. 29. $MnSi_{1.75}$. Dependence of the mass magnetization σ on the magnetic field H at 4.2 K, for magnetic fields perpendicular and parallel to the c axis [92V1].

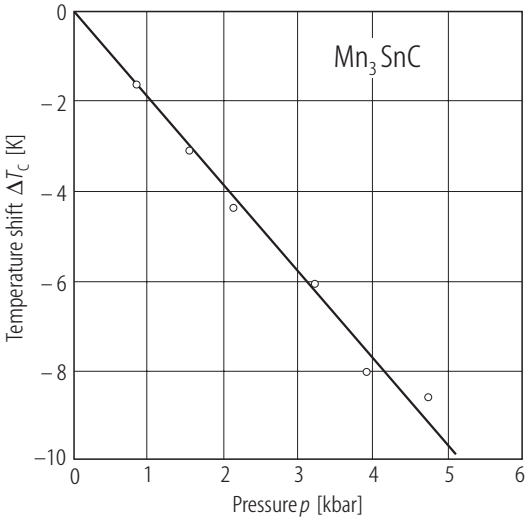

Fig. 31. Mn_3SnC. Shift of the Curie temperature, ΔT_C, under the influence of an applied pressure [87K3].

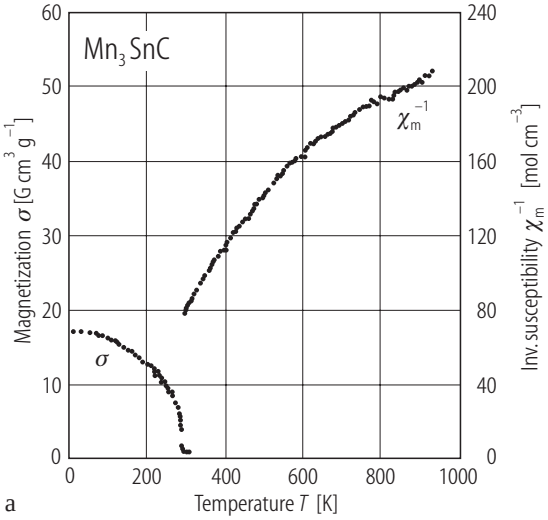

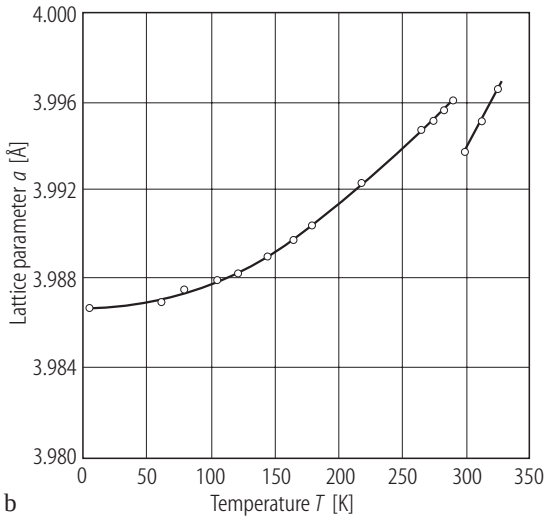

Fig. 30. Mn_3SnC. (**a**) Temperature dependence of the mass magnetization σ and the inverse molar magnetic susceptibility χ_m^{-1} measured in a magnetic field of 8.7 kOe [87K3, 93K2]. (**b**) Temperature dependence of lattice parameter a [72F1] of this compound which has a cubic, perovskite type of crystal structure.

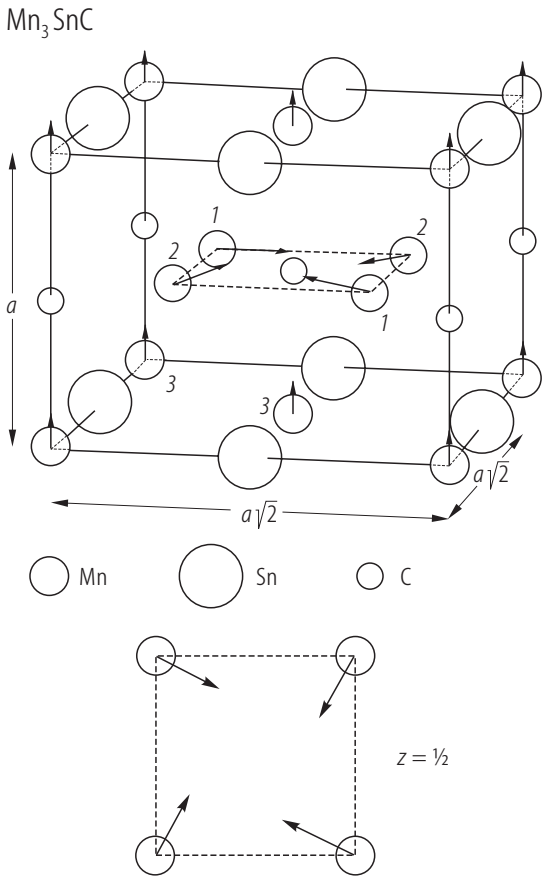

Fig. 32. Mn_3SnC. Magnetic structure. Mn1 and Mn2 atoms have magnetic moments of 2.4 μ_B each, which forms a "square configuration" with ferromagnetic components of 0.2 μ_B per Mn along the [001] direction, while Mn3 atoms have a magnetic moment of 0.65 μ_B aligned ferromagnetically along the [001] direction [78F2].

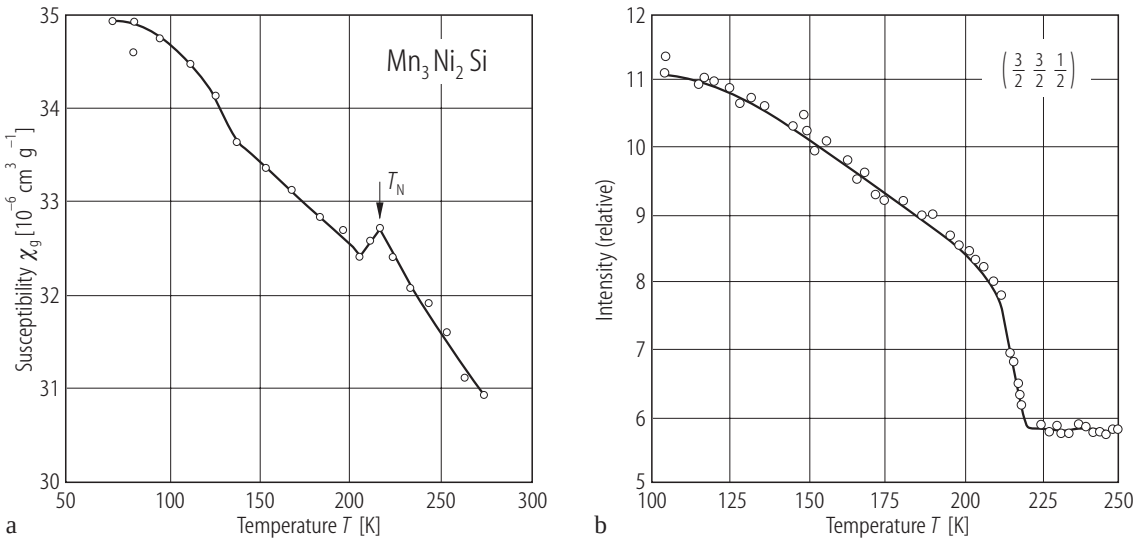

Fig. 33. Mn_3Ni_2Si. Temperature dependence of (**a**) the magnetic mass susceptibility χ_g and (**b**) the powder neutron diffraction intensity of the 3/2,3/2,1/2 magnetic line, from which a Néel temperature of 215 K is derived [90K2].

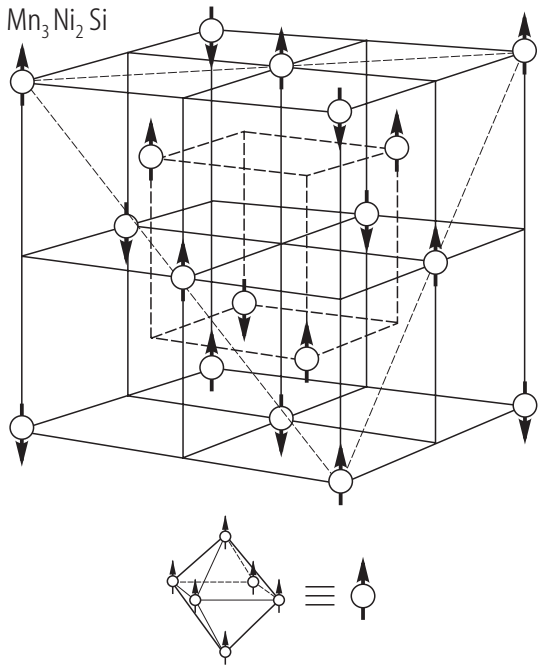

Fig. 34. Mn_3Ni_2Si. Magnetic structure. Each of the spheres forming a diamond structure represents a regular octahedron of Mn atoms in which the six atomic moments of 0.57 μ_B align ferromagnetically along the direction of the arrow [90K2]. Ni and Si atoms carry no magnetic moment and are not shown.

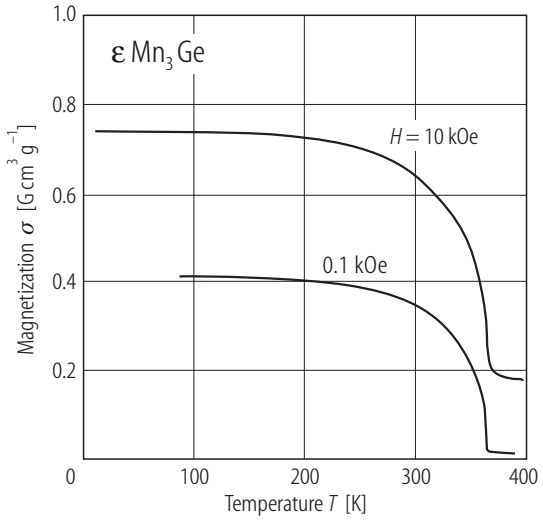

Fig. 37. εMn_3Ge (23.5 at% Ge). Temperature dependence of the mass magnetization σ measured in magnetic fields of 0.1 and 10 kOe [88Y2]. Single-phase specimen showing no low-temperature anomaly.

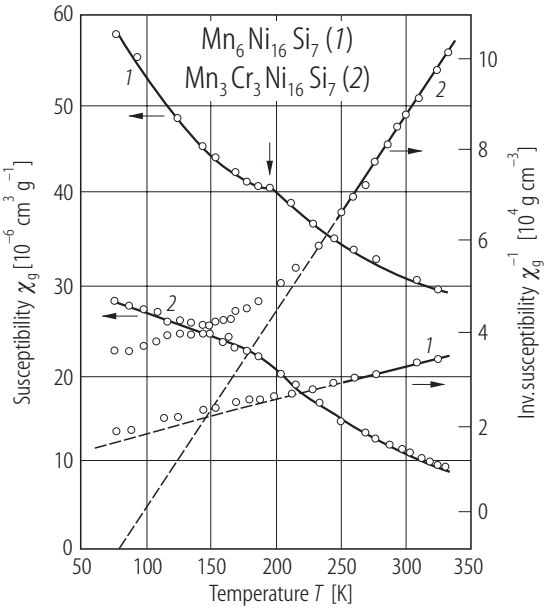

Fig. 35. $Mn_6Ni_{16}Si_7$, $Mn_3Cr_3Ni_{16}Si_7$. Temperature dependence of magnetic mass susceptibilities χ_g and their inverse values χ_g^{-1} [91K1].

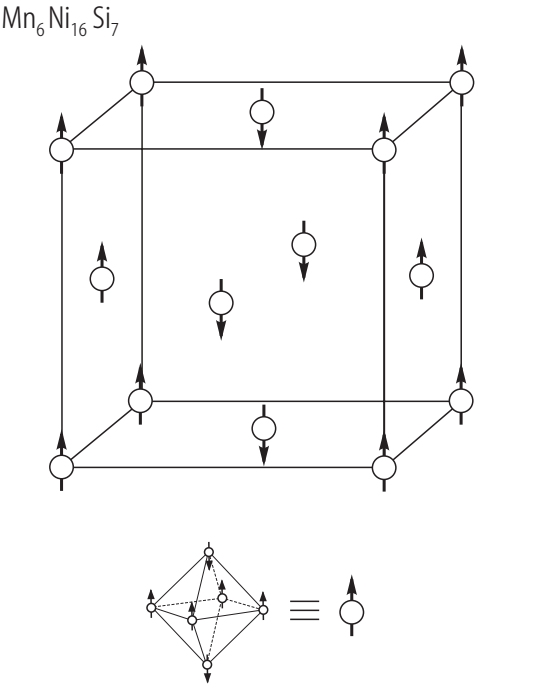

Fig. 36. $Mn_6Ni_{16}Si_7$. Magnetic structure. Only Mn atoms carry a magnetic moment (2.7 μ_B). Each of the spheres forming a face-centered structure represents a regular octahedron of Mn, in which 4 Mn moments in an *x-y* plane align along the positive *z* direction, while the other 2 Mn moments are oriented in the negative *z* direction [91K1].

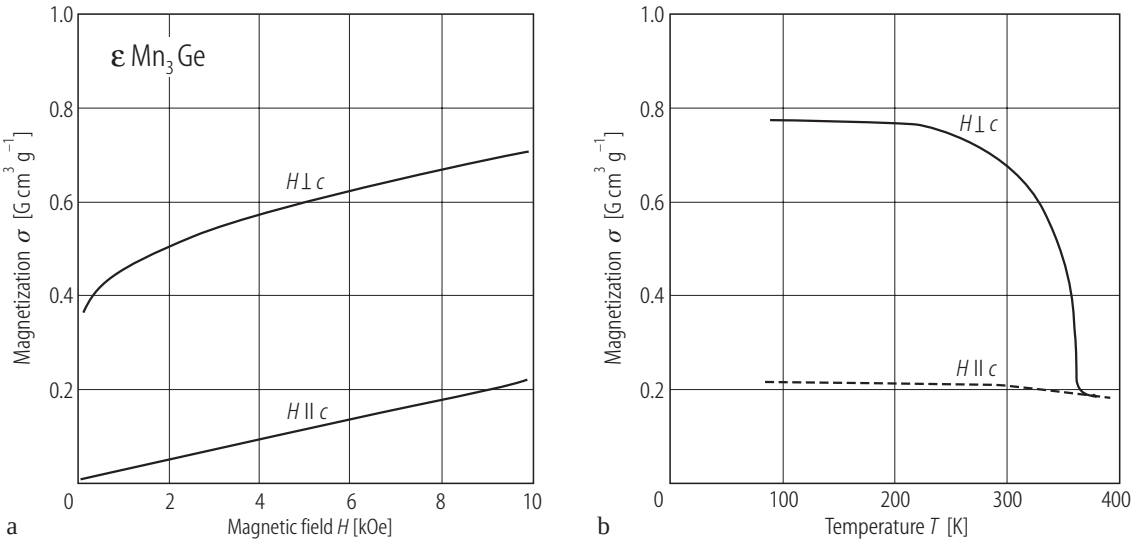

Fig. 38. εMn_3Ge (23.0 at% Ge). (**a**) Dependence of the mass magnetization σ on magnetic fields H oriented parallel or perpendicular to the hexagonal c axis at room temperature [88Y2]. (**b**) Temperature dependence of the mass magnetization σ in magnetic fields of 10 kOe parallel or perpendicular to c axis [90Y1].

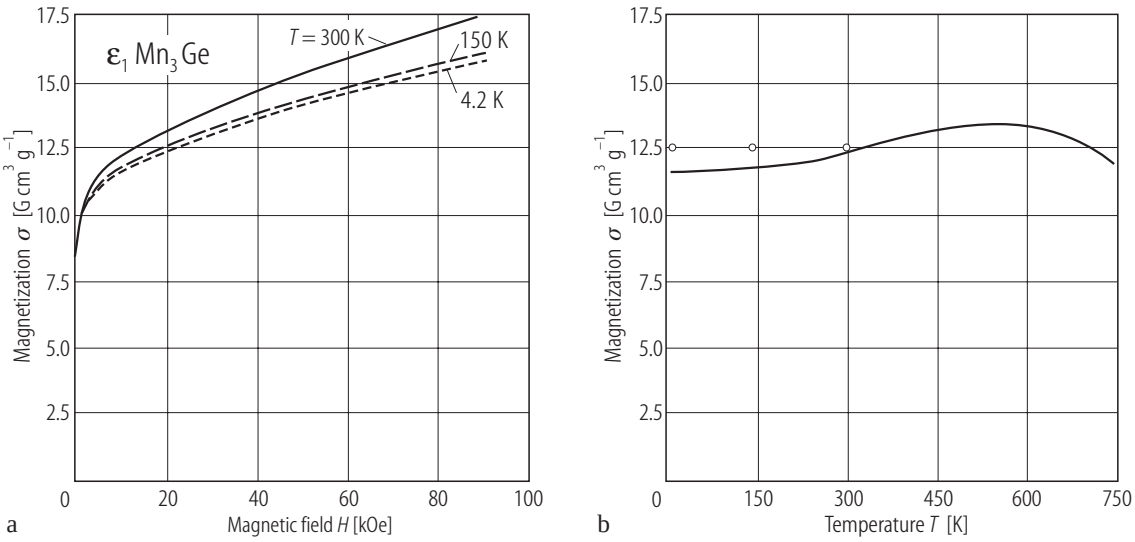

Fig. 39. $\varepsilon_1 Mn_3Ge$ (23.5 at% Ge). (**a**) Dependence of the mass magnetization σ on an applied magnetic field H at various temperatures [90Y1]. (**b**) Temperature dependence of the mass magnetization σ in an applied magnetic field of 10 kOe. Open circles: spontaneous magnetization obtained from (**a**) [90Y1].

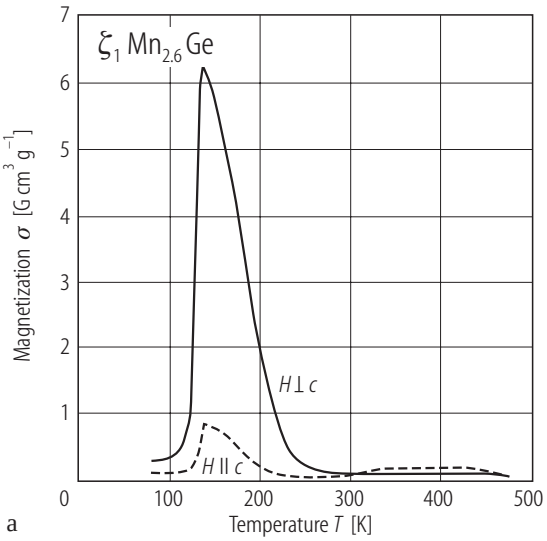

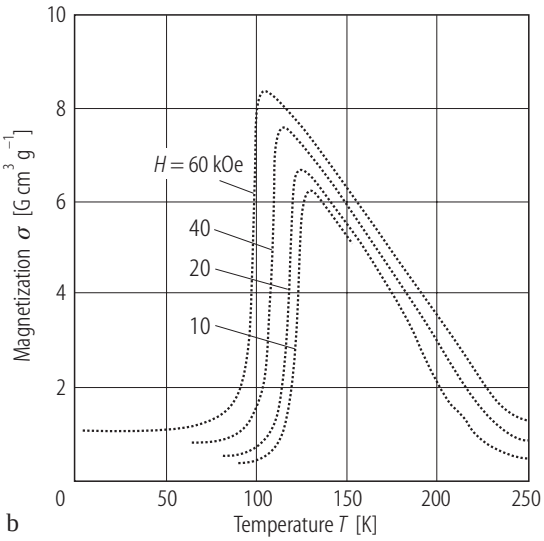

Fig. 40. $\zeta_1 Mn_{2.6}Ge$ (27.8 at% Ge). Temperature dependence of the mass magnetization (**a**) in a magnetic field of 10 kOe perpendicular or parallel to the trigonal *c* axis and (**b**) in various applied magnetic fields perpendicular to the *c* axis [88Y1]. Former specimens must have consisted of ζ_1 and ζ_2 subphases.

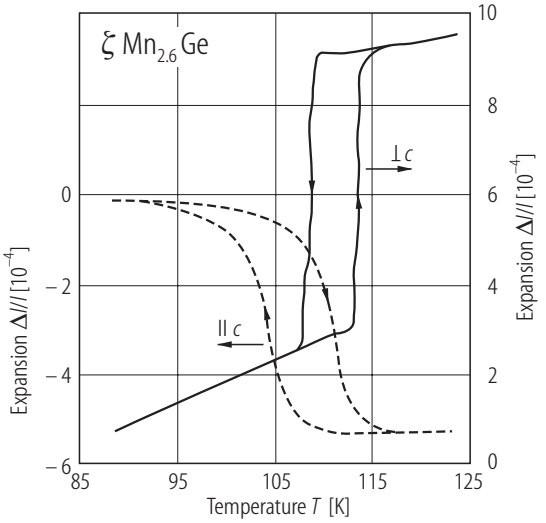

Fig. 41. $\zeta Mn_{2.6}Ge$ (28 at% Ge). Thermal hysteresis of the thermal expansions $\Delta l/l$ along and perpendicular to the trigonal *c* axis near the magnetic transition temperature of the ζ_1 subphase [87V1].

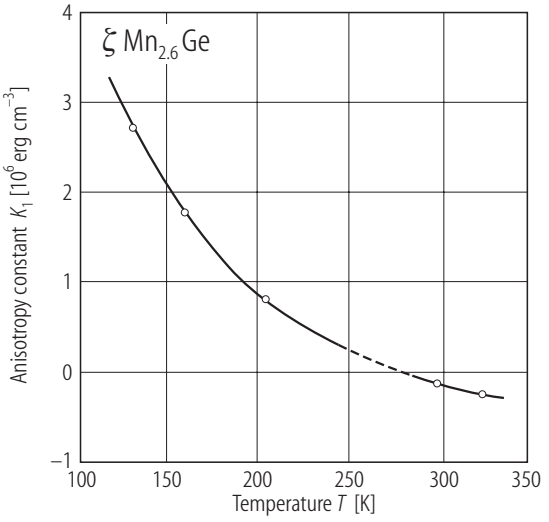

Fig. 42. $\zeta Mn_{2.6}Ge$ (28 at% Ge). Temperature dependence of the uniaxial magneto-crystalline anisotropy constant *K*, as determined from magnetization curves in magnetic fields perpendicular and parallel to the trigonal *c* axis [91T1]. The anisotropy in the lower and upper temperature ranges is due to the spontaneous magnetization of ζ_1 and ζ_2 subphases, respectively.

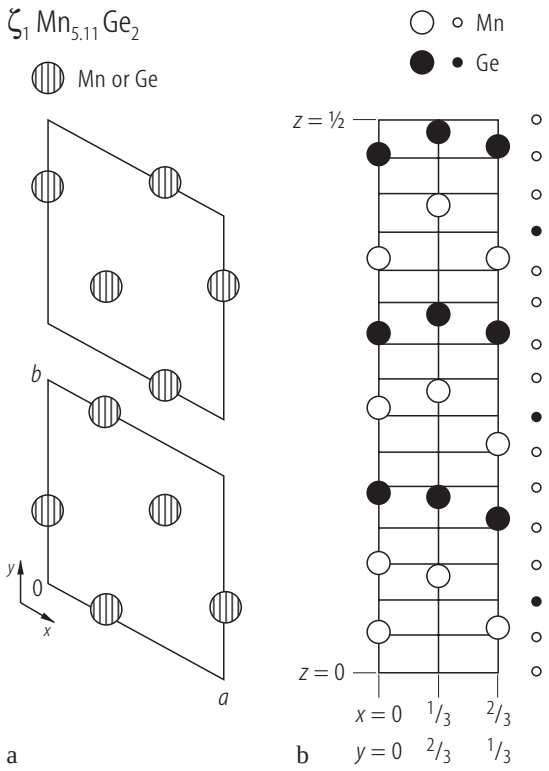

Fig. 43. $\zeta_1 Mn_{5.11}Ge_2$. Crystal structure. Trigonal crystal with hexagonal lattice. (**a**) Arrangement of the atoms in the fundamental layers, which are stacked alternatively along the *c* direction with an interlayer distance of ≈ *c*/30. (**b**) Half of the unit cell projected along the [010] direction. The fundamental layers and the three-fold axes are represented by horizontal and vertical lines, respectively. Atoms on the three-fold axes are represented by larger circles. The kind of atoms in the fundamental layers are shown by small circles along side of the figure. The unit cell contains 92 Mn and 36 Ge atoms [87K1, 87K2].

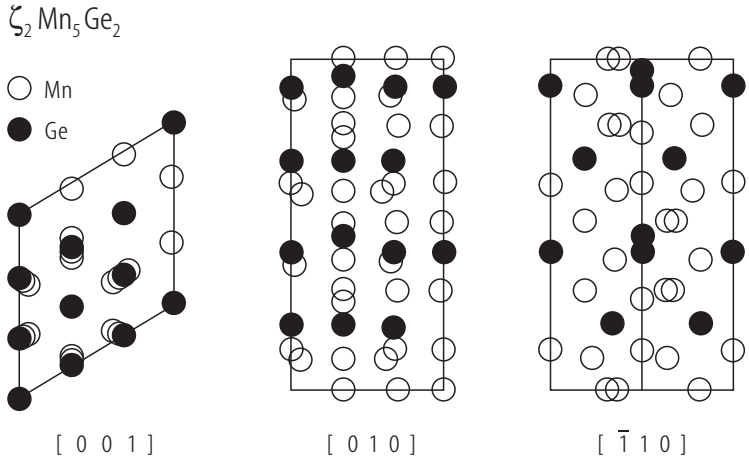

Fig. 44. $\zeta_2 Mn_5Ge_2$. Crystal structure. Projections of the hexagonal unit cell containing 30 Mn and 12 Ge atoms along the [001], [010] and [$\bar{1}$10] directions. The structure was determined using a mixed crystal of ζ_1 and ζ_2, because the latter is always obtained as an intergrowth with the former, having common crystal axis ***a*** with $\boldsymbol{c}_1 = 3\boldsymbol{c}_2$, where $\boldsymbol{c}_1$ and $\boldsymbol{c}_2$ are the ***c*** axis of ζ_1 and ζ_2 subphases, respectively [87K2, 87O1].

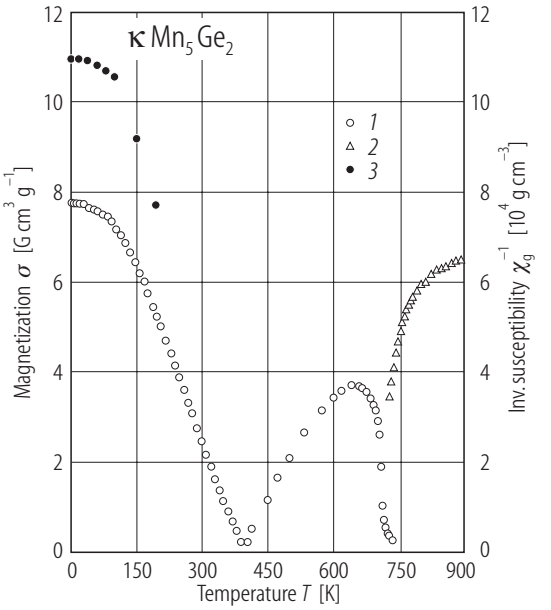

Fig. 45. κMn_5Ge_2. Temperature dependence of the mass magnetization σ (*1*) in a magnetic field of 7.5 kOe, the inverse mass susceptibility χ_g^{-1} (*2*) and also the spontaneous magnetization σ_s (*3*) derived from high-field isothermal magnetization curves [85Y1].

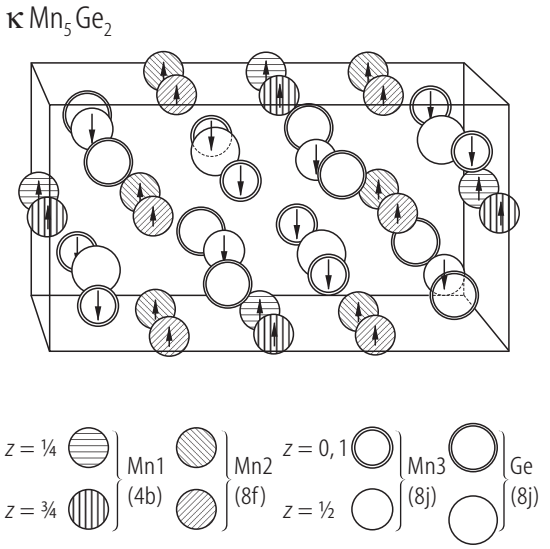

Fig. 46. κMn_5Ge_2. Crystallographic and magnetic structures [84O2, 87Y1]. Perspective view of the orthorhombic unit cell along the *c* direction, with the *a* axis horizontal. Magnetic moments are collinearly oriented along the *b* axis.

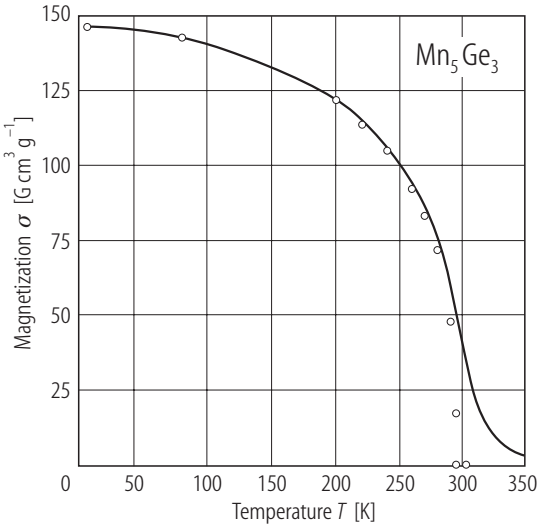

Fig. 47. ηMn_5Ge_3. Temperature dependence of the mass magnetization σ measured in a magnetic field of 10 kOe along the *c* axis which is the direction of easy magnetization. Open circles: spontaneous mass magnetization derived from isothermal magnetization curves [90Y1].

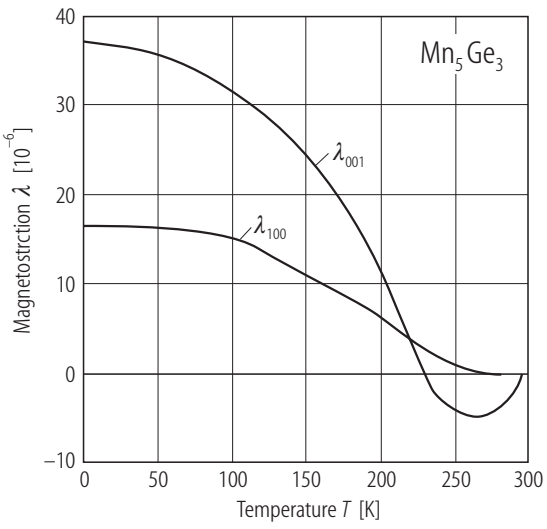

Fig. 48. ηMn_5Ge_3. Temperature dependence of the magnetostriction constants, λ_{001} and λ_{100} [91B1].

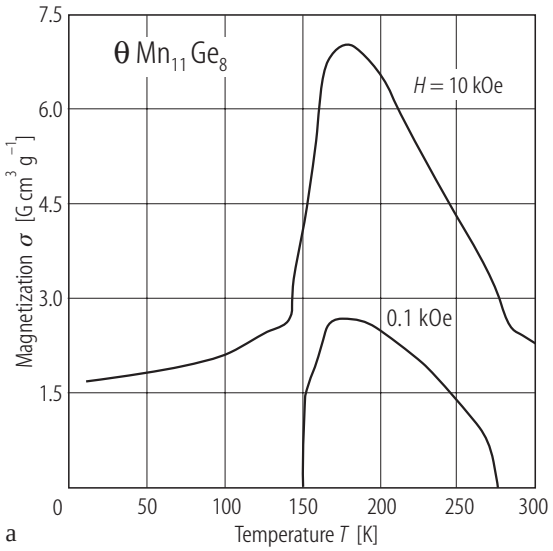

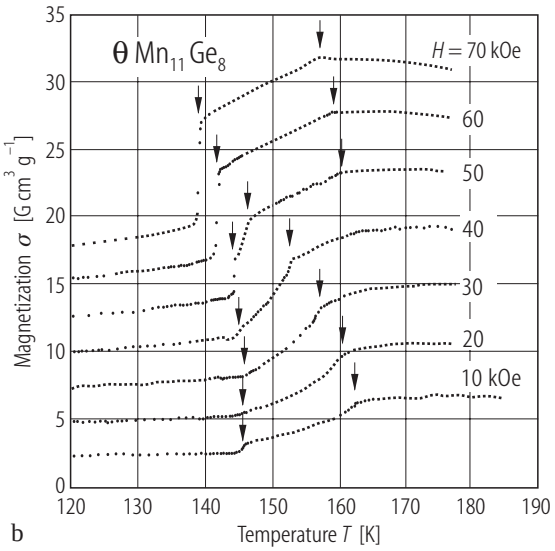

Fig. 49. $\theta Mn_{11}Ge_8$. Temperature dependence of the mass magnetization σ measured in magnetic fields of (**a**) 0.1 and 10 kOe and (**b**) up to 70 kOe oriented along the *b* axis [86Y1, 89Y1].

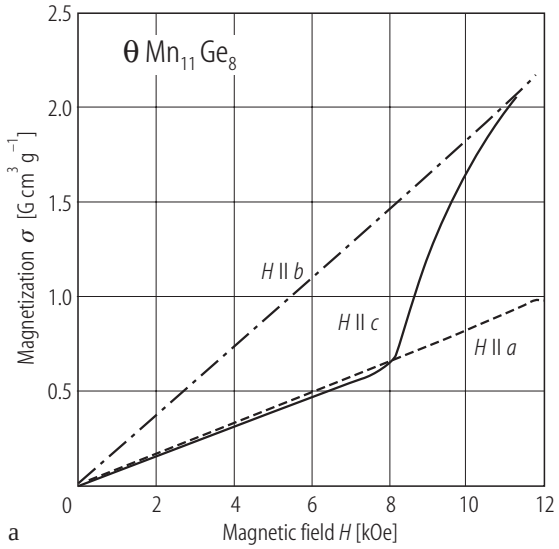

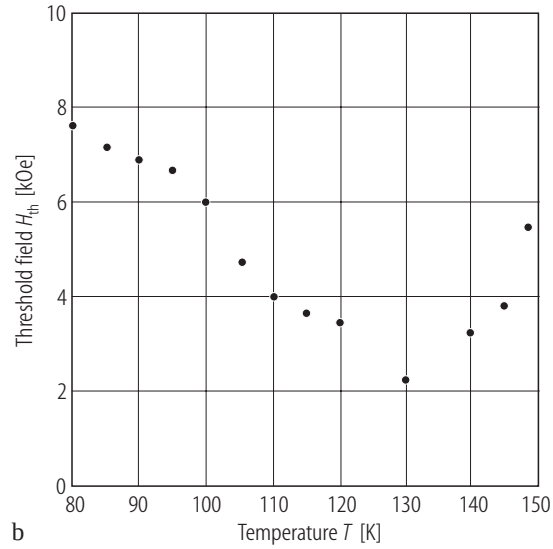

Fig. 50. $\theta Mn_{11}Ge_8$. (**a**) Dependence of the mass magnetization σ on the static magnetic fields *H* along *a*, *b* and *c* axes at 80 K [86Y1]. A spin flop is seen for the field parallel to the *c* axis. (**b**) Temperature dependence of the threshold magnetic field H_{th} along the *c* axis at which the spin flop starts [86Y1].

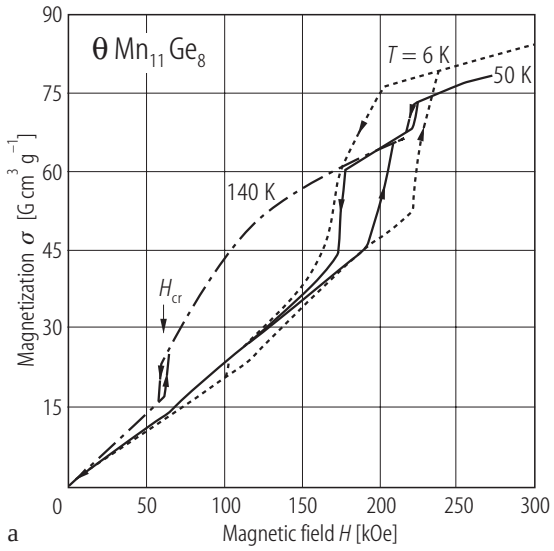

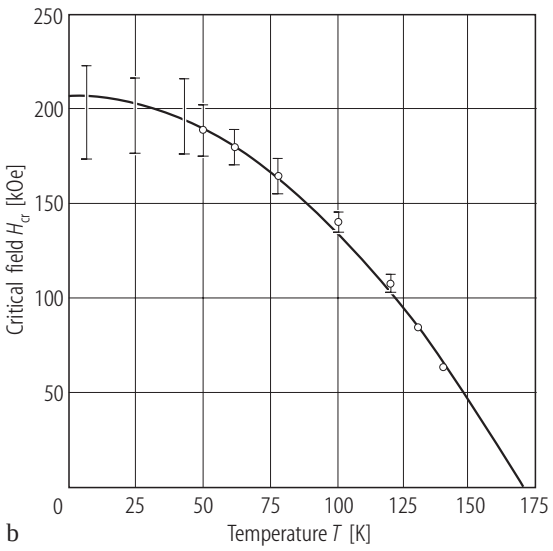

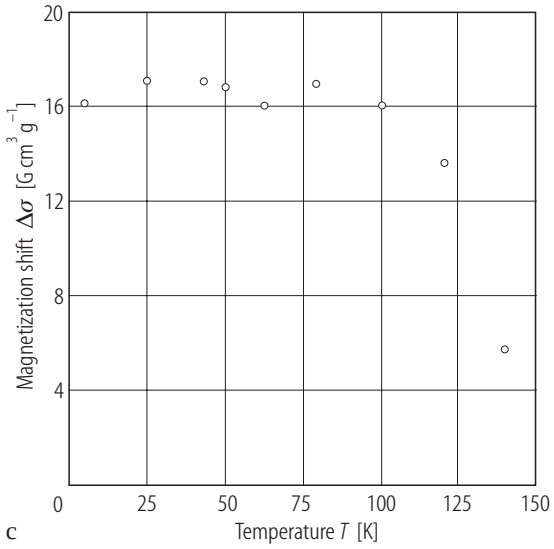

Fig. 51. θ$Mn_{11}Ge_8$. (**a**) Field dependence of the mass magnetization σ in a pulsed magnetic field along the *b* axis at 140, 50 and 6 K [89Y1]. (**b**) Temperature dependence of the critical field along the *b* axis for the field-induced AF-F transition. Vertical line segments indicate the range of magnetic hysteresis [89Y1]. (**c**) Temperature dependence of the jump in magnetization along the *b* axis at the AF-F transition [89Y1].

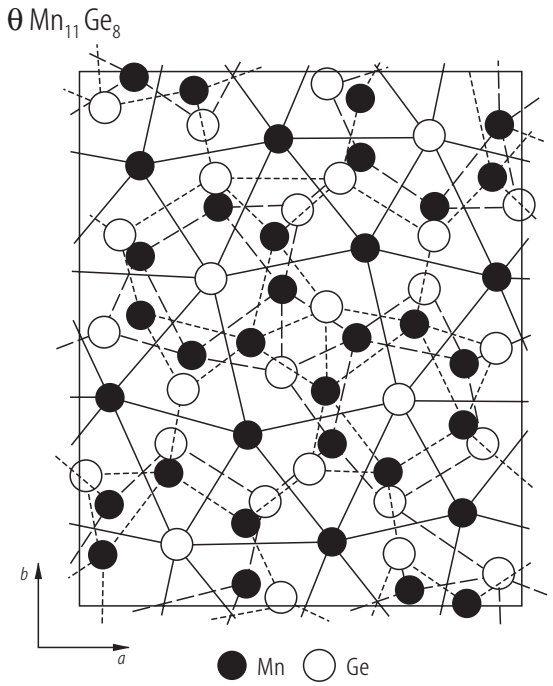

Fig. 52. θ$Mn_{11}Ge_8$. Crystal structure. The ***c*** projection of the orthorhombic unit cell. Full line: $z \approx 0$, 1/2; long-dashed line: $z = 1/4$; short-dashed line: $z = 3/4$ [84O1].

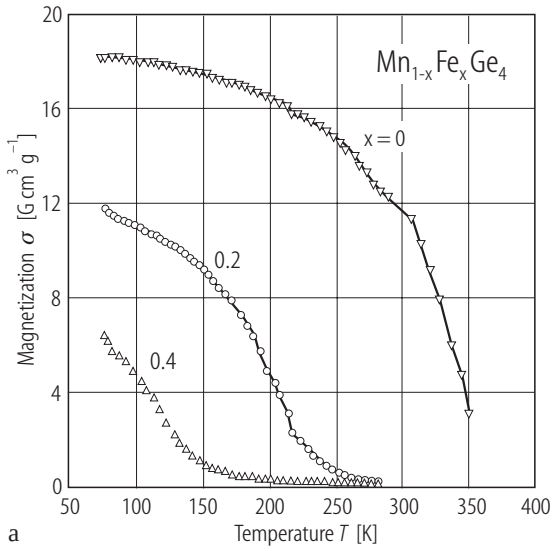

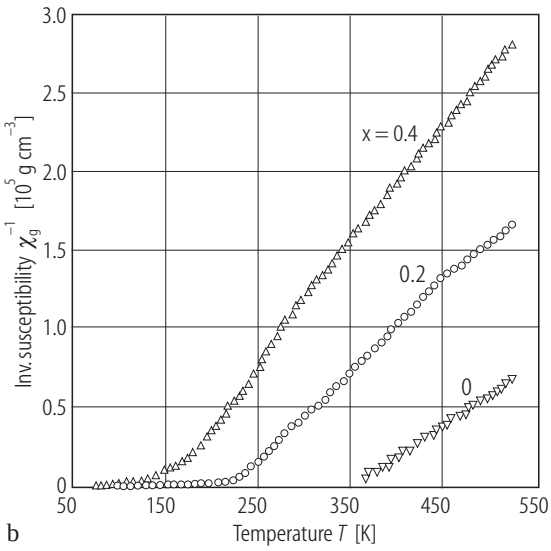

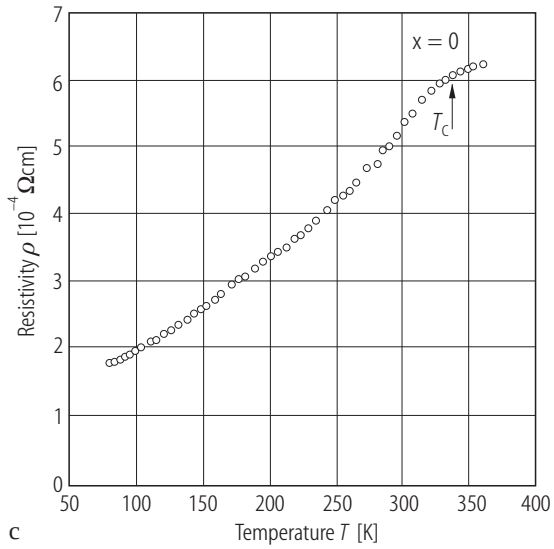

Fig. 53. $Mn_{1-x}Fe_xGe_4$ high-pressure synthesized. Temperature dependence of (**a**) the mass magnetization σ in a magnetic field of 10 kOe [93T1], (**b**) the reciprocal magnetic mass susceptibility χ_g^{-1} [93T1], and (**c**) the electrical resistivity ρ for x = 0, $MnGe_4$ [90T1].

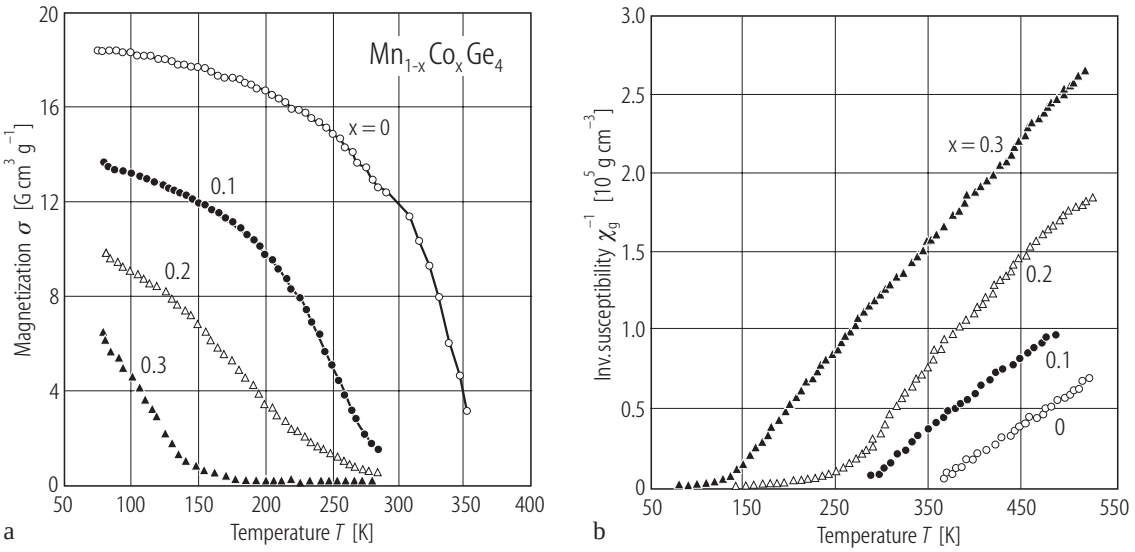

Fig. 54. $Mn_{1-x}Co_xGe_4$ high-temperature synthesized. Temperature dependence of (**a**) the mass magnetization σ in a magnetic field of 10 kOe, and (**b**) the reciprocal magnetic mass susceptibility χ_g^{-1} [93T1].

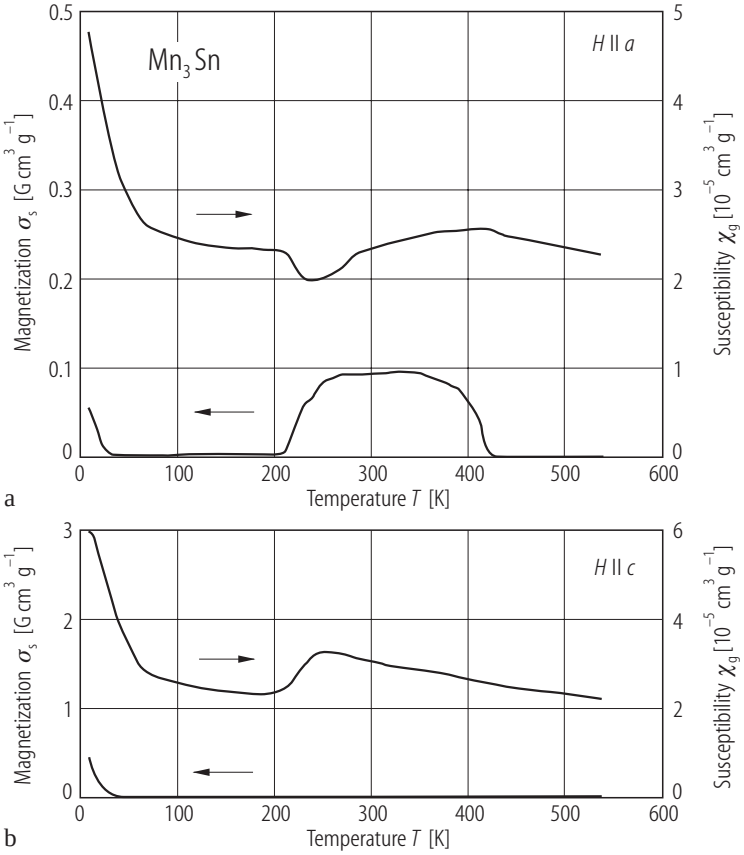

Fig. 55. Mn_3Sn. Temperature dependence of the spontaneous mass magnetization σ_s and the magnetic mass susceptibility χ_g [87O2]. (**a**) For magnetic field parallel to the *a* axis. (**b**) For magnetic field parallel to the *c* axis. The specimen has the composition $Mn_{3.6}Sn$ and was annealed at 850 °C for 50 h and cooled down to room temperature at 10 K/h.

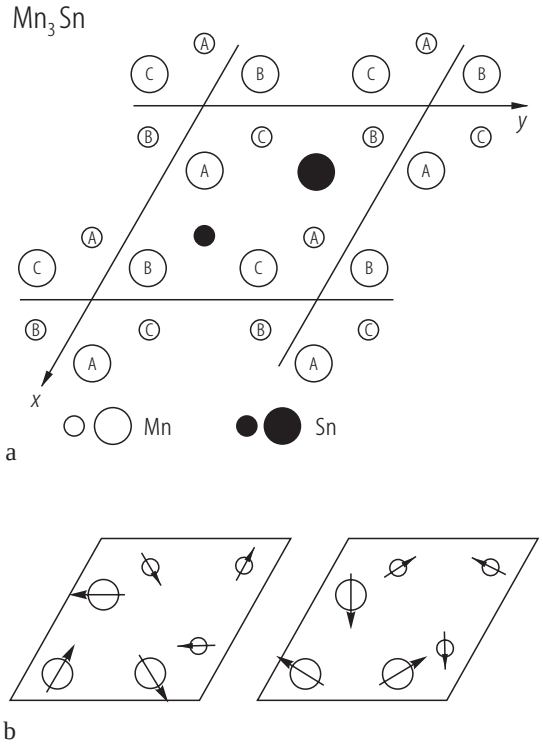

Fig. 56. Mn_3Sn. Magnetic structure determined at 200 K using generalized neutron polarization analysis on a single crystal with the composition $Mn_{3.2}Sn$ [90B2]. The *c* projection of the hexagonal $D0_{19}$ structure is shown in (**a**). Here Mn atoms are shown as open circles, while Sn atoms are shown as solid circles, the larger being at $z = 1/4$, the smaller at $z = 3/4$ for both Mn and Sn. Magnetic moments of Mn atoms on the three sublattices A, B and C essentially compensate making an equilateral triangle, in either of the two "inverse triangle" patterns shown in (**b**).

For Fig. 57 see p. 34

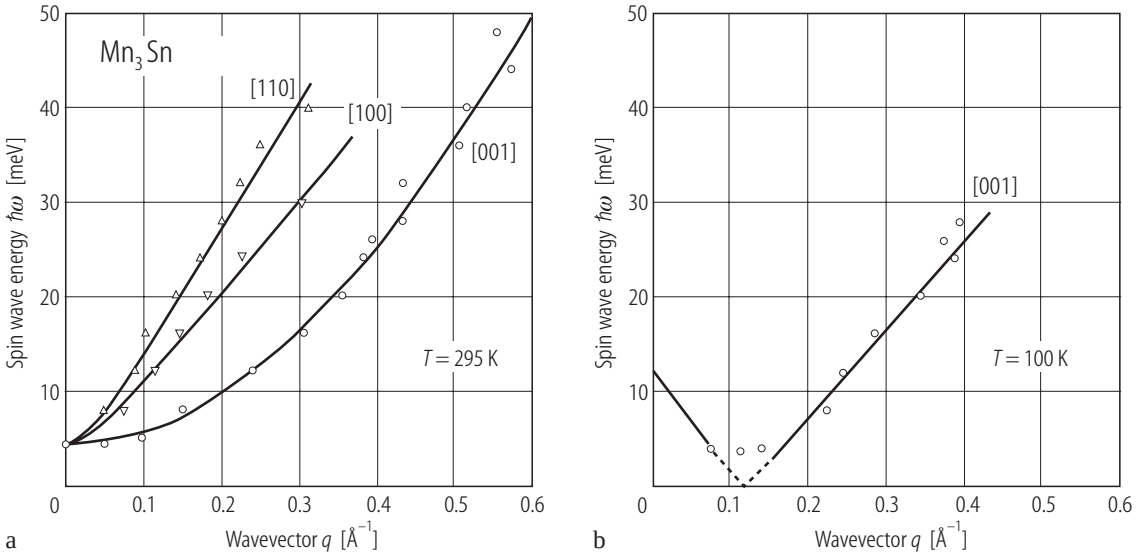

Fig. 58. Mn_3Sn. Spin-wave dispersion relations. Energy transfer vs. relative wave vector at temperatures 295 K (triangular phase) and 100 K (modulated phase), obtained through neutron inelastic scattering experiments on a specimen with composition $Mn_{3.2}Sn$ [92R1]. (**a**) dispersion relation at 295 K for relative wave vectors *q* parallel to [110], [100] and [001] reciprocal-lattice directions. (**b**) dispersion relation at 100 K for *q* parallel to [001].

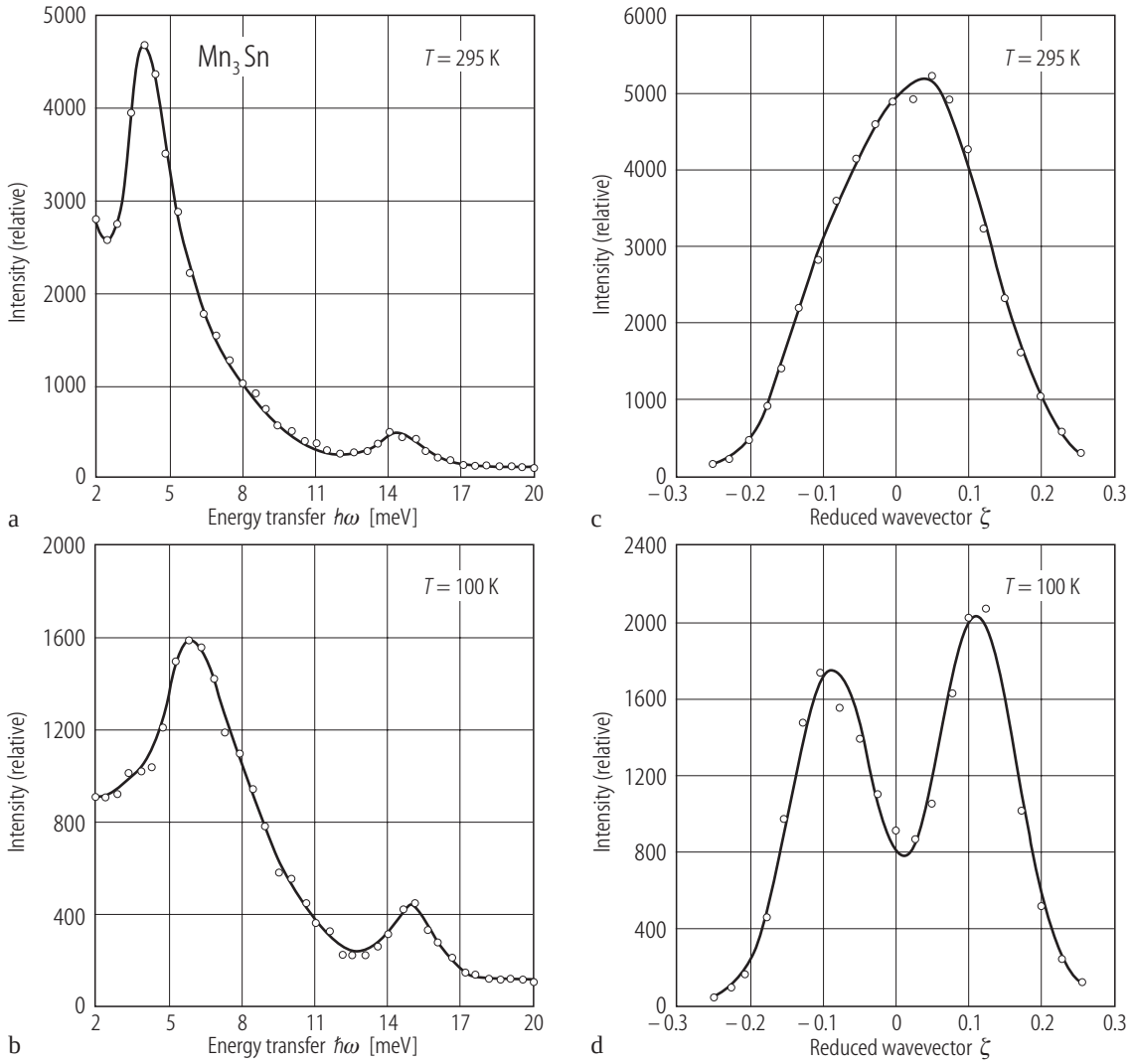

Fig. 57. Mn_3Sn. Magnetic excitation spectra around the reciprocal lattice point (110) obtained through inelastic neutron scattering at temperatures 295 K (triangular phase) and 100 K (modulated phase) [93C2]. (**a**) Neutron intensity vs. energy transfer $\hbar\omega$ (constant-Q) at (110) at 295 K. (**b**) Same as (**a**) but at 100 K. (**c**) Neutron intensity vs. ζ in (11ζ) (constant-E) for $\hbar\omega$ =4 meV at 295 K. (**d**) Same as (**c**) but at 100 K.

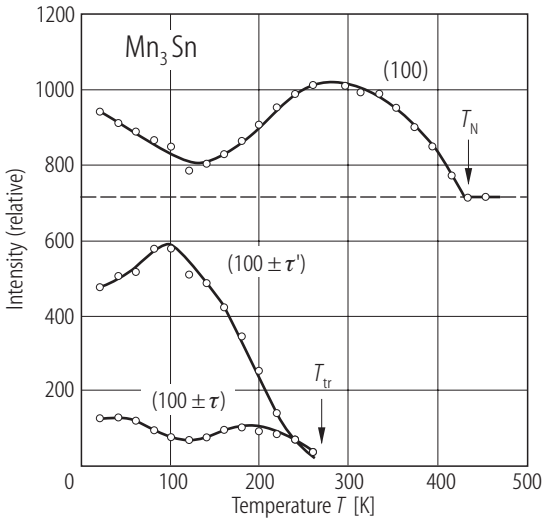

Fig. 59. Mn_3Sn. Temperature dependence of the integrated intensity of neutron diffraction, for fundamental and satellite reflections of (100). Data are obtained for an energy of 14.83 meV for a single-crystal specimen with composition $Mn_{3.2}Sn$ annealed at 850 °C for 50 h and cooled to room temperature at a rate of 10 K/h [93C1].

For Fig. 60 see p. 36

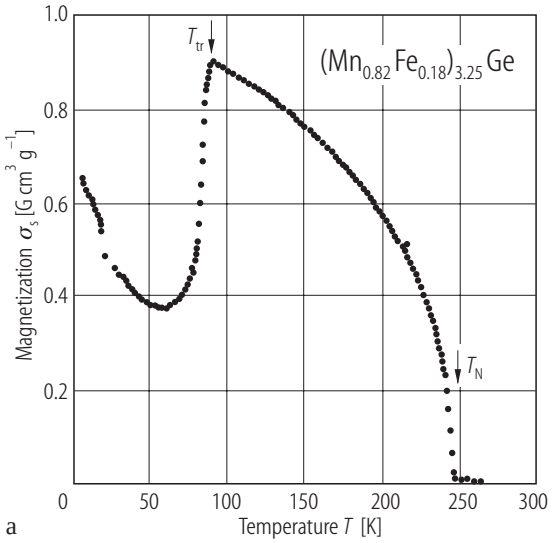

a

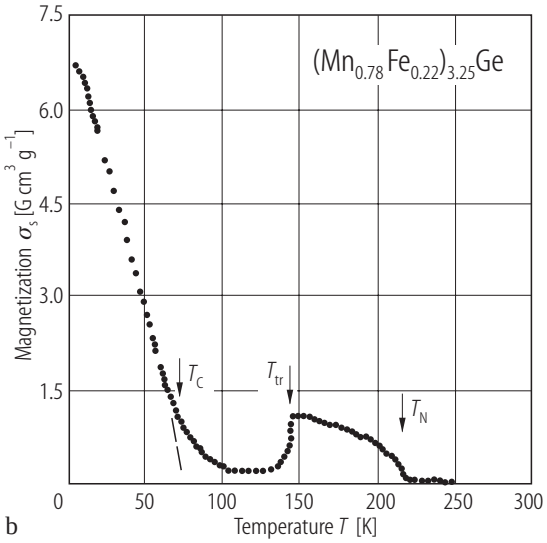

b

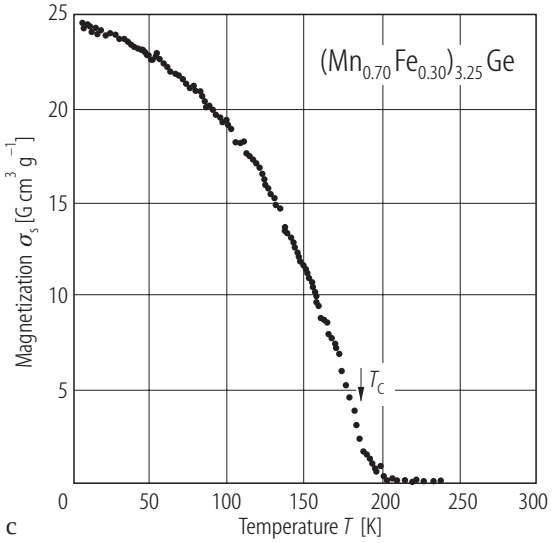

c

Fig. 61. $(Mn_{1-x}Fe_x)_{3.25}Ge$. Temperature dependence of saturation magnetization for x = 0.18, 0.22 and 0.30 [92H2].

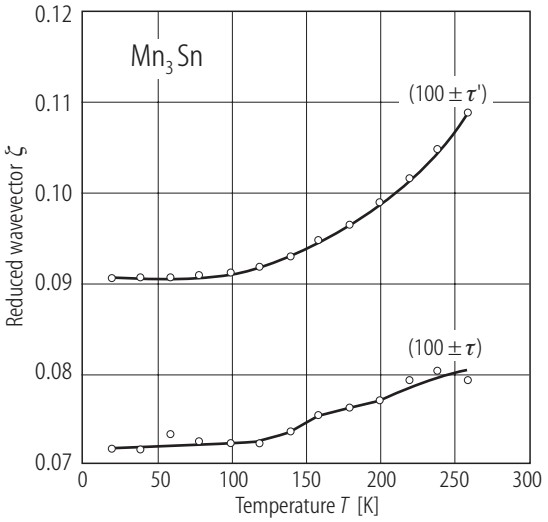

Fig. 60. Mn_3Sn. Temperature dependence of the peak positions of two pairs of satellite reflections in reciprocal lattice unit, $\zeta = 0$ corresponding to the fundamental (100) position [93C1]. The specimen is the same that was used for Fig. 59.

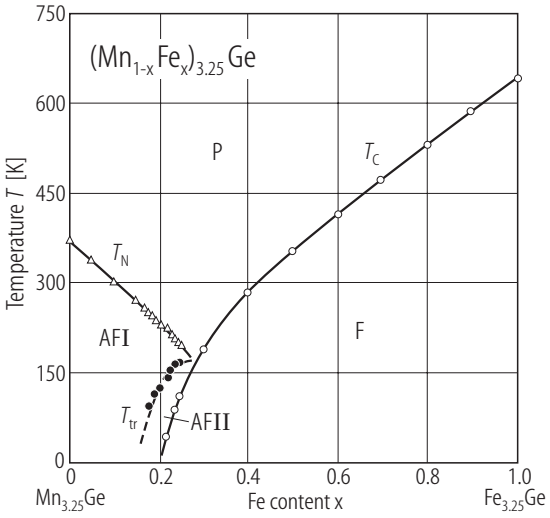

Fig. 62. $(Mn_{1-x}Fe_x)_{3.25}Ge$. Magnetic phase diagram in a composition - temperature plane. P: paramagnetic; F: ferromagnetic; AF: antiferromagnetic. AFI: triangular spin arrangement in the *c* plane; AFII: collinear; parallel spin arrangement within a *c* plane with antiparallel coupling between *c* planes [92H2].

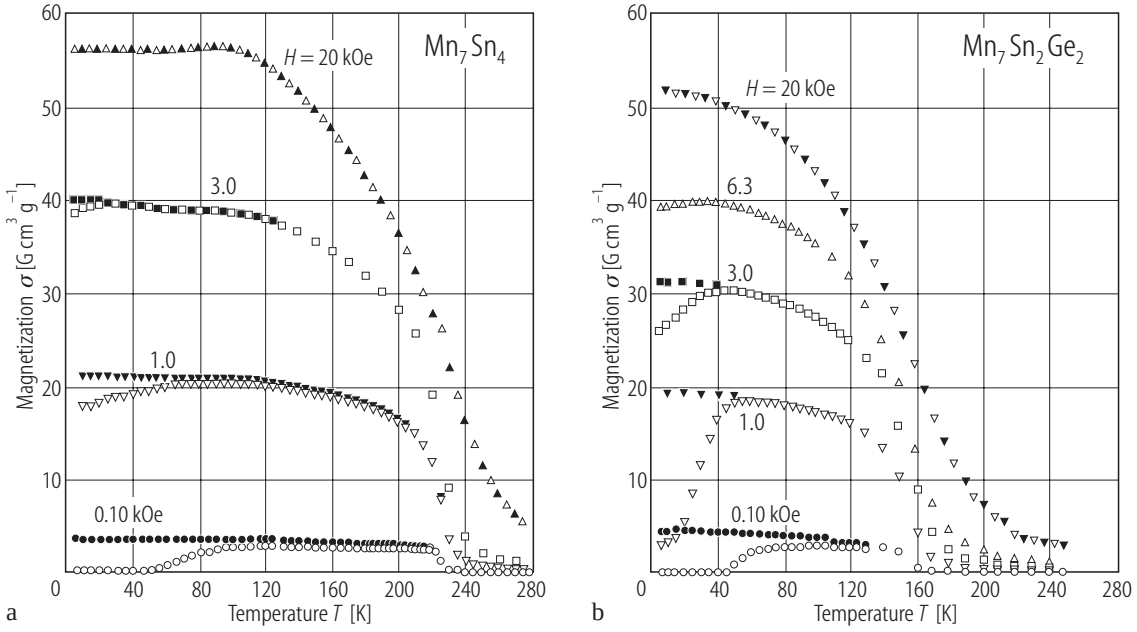

Fig. 64. $Mn_7(Sn_{1-x}Ge_x)_4$. Temperature dependence of the mass magnetization σ for (**a**) x = 0 (Mn_7Sn_4) and (**b**) x = 0.50 ($Mn_7Sn_2Ge_2$) as measured in various magnetic fields *H*. Heating run after the sample was cooled in zero field (open symbols) and cooled in magnetic field (solid symbols) which is equal to the measuring field indicated [93H1].

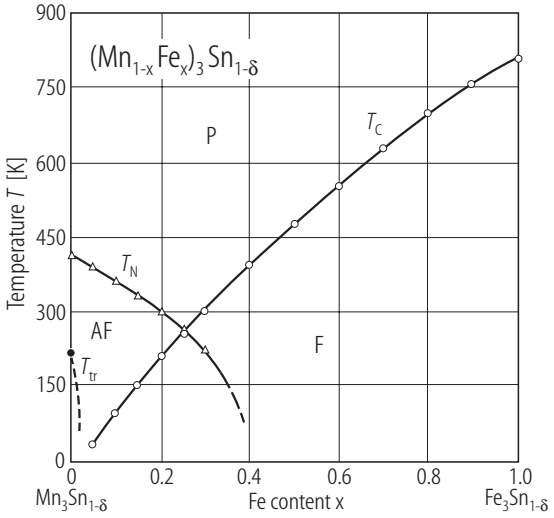

Fig. 63. $(Mn_{1-x}Fe_x)_3Sn_{1-\delta}$. Magnetic phase diagram in composition - temperature plane. Néel temperature T_N, Curie temperature T_C and another magnetic transition temperature T_{tr} are shown as functions of composition. $\delta = 0 \ldots 0.10$. The dependences on δ are too small to be shown in the figure except for T_{tr}. $T_{tr} = 284$ K for $(x,\delta) = (0,0)$, $T_{tr} = 220$ K for (0,0.05) and $T_{tr} < 77$ K for (0.02, 0.1) [90H1, 93H2]. P: paramagnet; F: ferromagnet; AF: antiferromagnet.

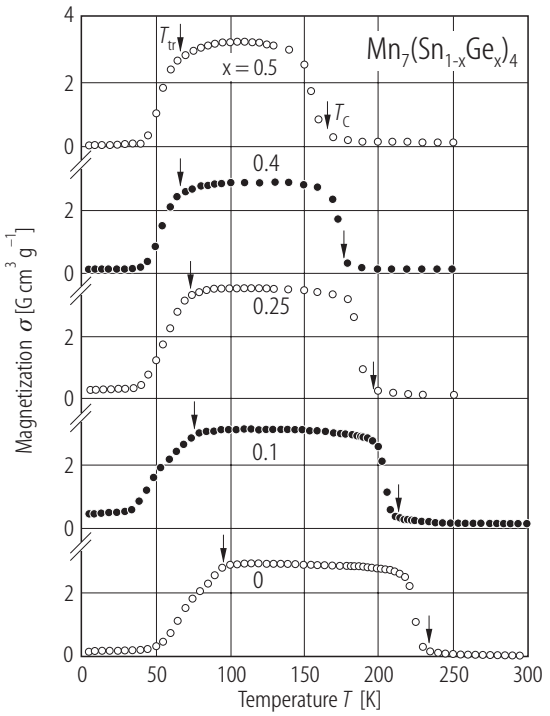

Fig. 65. $Mn_7(Sn_{1-x}Ge_x)_4$. Temperature dependence of the mass magnetization σ in a magnetic field of 0.10 kOe for various compositions x. Heating run after the samples were cooled in zero magnetic field. T_C: ferri-magnetic Curie temperature; T_{tr}: transition temperature from low-temperature spin-glass-like state to collinear ferrimagnetic state [93A3].

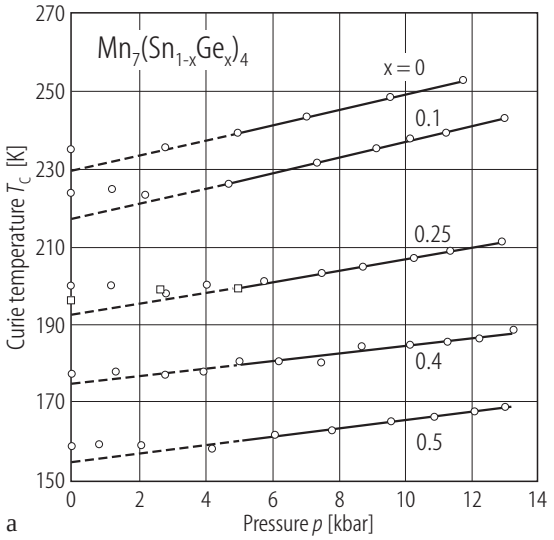

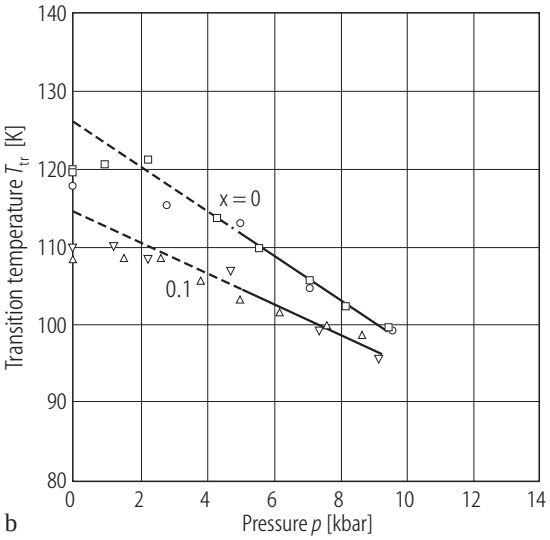

Fig. 66. $Mn_7(Sn_{1-x}Ge_x)_4$. (**a**) Pressure dependence of the ferrimagnetic Curie temperature T_C for various compositions x. Squares represent the data in the second run. (**b**) Pressure dependence, for x = 0 and 0.1, of the transition temperature T_{tr} from low-temperature spin-glass-like state to ferrimagnetic state. Different symbols correspond to different runs [93O1].

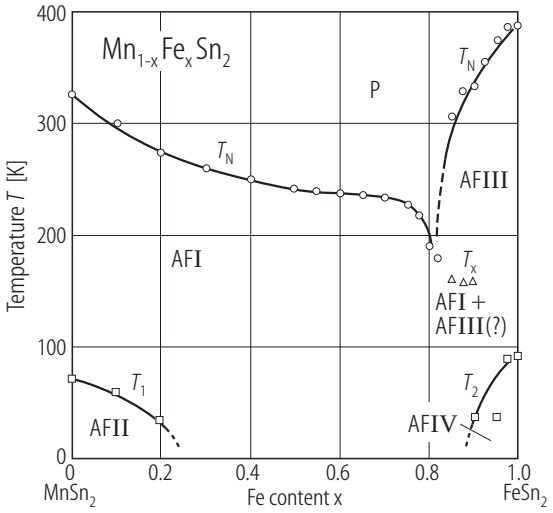

Fig. 67. $Mn_{1-x}Fe_xSn_2$. Magnetic phase diagram in composition - temperature plane [93S4]. P: paramagnetic; AF: antiferromagnetic. I to IV label the magnetic-structure types. In the first two, the atomic moments align parallel within each of (110) planes, which, in turn, are arranged as + – + – in type I but as + + – – in type II. Types III and IV are those shown in Fig. 107 (a) and (b), respectively.

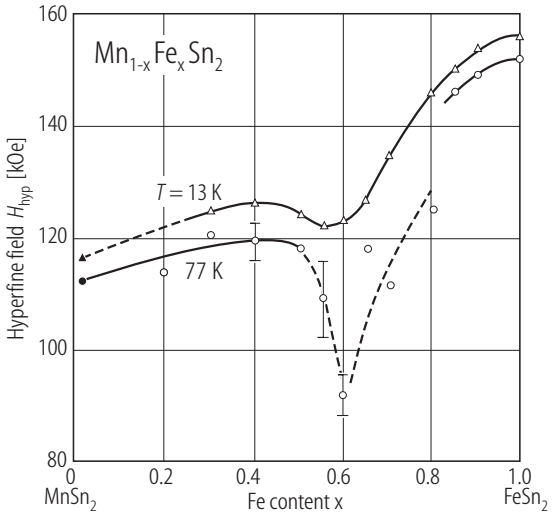

Fig. 68. $Mn_{1-x}Fe_xSn_2$. Hyperfine field H_{hyp} at ^{57}Fe at 13 K and 77 K plotted against the composition parameter x. Solid symbols show the values obtained by [82L1] at 86 K and 4.2 K, respectively [93S2, 93S4].

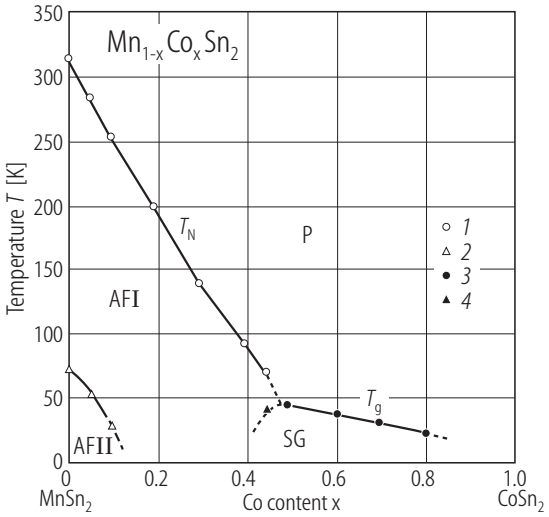

Fig. 69. $Mn_{1-x}Co_xSn_2$. Magnetic phase diagram in a composition - temperature plane. The data were obtained from dc (*1*, *2*) and ac (*3*) susceptibility measurements. The temperature below which the field cooling effect is observed is also plotted (*4*) [90S1]. P: paramagnetic; SG: spin glass; AF: antiferromagnetic. Magnetic structure types I and II are described in the caption of Fig. 67.

1.5.4.5 Fe alloys and compounds

1.5.4.5.1 Alloys and compounds with C and Si

The $Fe_{3-x}Mn_xSi$ system has attracted much attention, since in this range Fe_3Si is ferromagnetic, the Heusler alloy Fe_2MnSi has a complex magnetic behaviour, and Mn_3Si is antiferromagnetic.